Mathematics in Applied Sciences and Engineering
Online First, pp.**1-23**

https://ojs.lib.uwo.ca/mase
https://doi.org/10.5206/mase/23120

THERMAL IRREVERSIBILITY AND BIO-CONVECTIVE TRANSPORT IN A RADIATIVE WILLIAMSON HYBRID NANOFLUID: APPLICATION TO SOLAR-POWERED AIRCRAFT

MUHAMMAD NAVEED SANI, MUHAMMAD SAGHEER, HASSAN SHAHZAD, AND MUHAMMAD SAMIULLAH

Abstract. Solar energy, as the primary source of thermal radiation, plays a pivotal role in powering photovoltaic systems, solar panels, and advanced energy applications including hybrid nanofluids. With the growing integration of nanotechnology into aerospace systems, researchers are actively exploring its potential to enhance the thermal performance and operational efficiency of solar-powered aircraft. This study investigates the heat and mass transfer characteristics of both mono nanofluid (Cu/SA) and hybrid nanofluid (GO–Cu/SA) flowing over an extendable surface. The hybrid nanofluid is directed toward a parabolic trough embedded within the wings of a solar-powered aircraft, simulating realistic aerospace thermal conditions. Key effects such as viscous dissipation, inclined magnetic field, and thermal radiation are considered to evaluate heat transfer efficiency. Additionally, entropy generation in the flow of a Williamson hybrid nanofluid over an extensible sheet is analyzed to assess thermal irreversibility. The governing partial differential equations, derived from conservation laws, are transformed into ordinary differential equations (ODEs) using similarity variables. These ODEs are then solved numerically using the shooting method. The working fluid comprises sodium alginate as the base liquid, with copper and graphene oxide nanoparticles uniformly dispersed. Results are presented through graphical and tabular formats to illustrate variations in velocity, temperature, concentration, and motile microorganism density. Findings reveal that the Biot number enhances the heat transfer rate by approximately 40.60%–86.54% for the mono nanofluid (Cu/SA) and 39.90%–85.67% for the hybrid nanofluid (GO–Cu/SA). Moreover, the chemical reaction parameter increases the mass transfer rate by 21.53% in the mono nanofluid and 16.40% in the hybrid nanofluid. It is also observed that an increase in the velocity slip parameter leads to a reduction in entropy generation. The obtained results are validated against existing literature, confirming their accuracy and reliability.

1. Introduction

Nanofluids, introduced by Choi and Eastman [11], represent a class of fluids engineered by dispersing nanoscale particles into base liquids like water or oil to enhance thermal properties. Their exceptional heat transfer performance and thermal conductivity have made them ideal candidates in solar energy systems. Rubbi et al. [26] further advanced the domain by employing MXene (Ti_3C_2) particles suspended in soybean oil, which yielded the highest thermal efficiency compared to conventional fluids. These findings support the idea that nanoparticle type and base fluid selection directly affect energy system performance. Subramani et al. [34] observed a 3% improvement in solar collector efficiency by introducing Al_2O_3 nanoparticles at only a 0.05% volume fraction. Later, Abdelrazik et al. [2] conducted a practical study using nanofluid-based optical filters to boost the thermal efficiency of hybrid photovoltaic/thermal (PV/T) systems. They demonstrated that tailoring nanofluid properties could significantly improve spectral selectivity and thermal output. Extending the scope of application, Yousaf et al. [41] investigated a bio-convective nanofluid incorporating motile microorganisms and activation

Received by the editors 23 June 2025 ; accepted 11 November 2025; published online 24 November 2025.
Key words and phrases. Non-Newtonian hybrid fluid flow, shooting method, irreversibility analysis, solar aircraft, heat and mass transfer phenomenon.

energy under Magnetohydrodynamics (MHD) and nonlinear thermal radiation, demonstrating its relevance in surface heating and aerospace-inspired fluid systems. Farooq et al. [**?**] employed the bvp4c solver and reported that an increase in the magnetic parameter enhances heat and mass transfer rates over a nonlinear stretching sheet. Thenmozhi et al. [37] used the shooting method and concluded that higher Jeffrey parameter values lead to increased momentum diffusion and a corresponding reduction in nanofluid velocity.

Hybrid nanofluids extend the capabilities of single-component nanofluids by incorporating multiple types of nanoparticles to exploit their combined thermal and physical advantages. Sidik et al. [**?**] presented a comprehensive review of hybrid nanofluids, highlighting their superior thermal performance, stability, and economic advantages. Huminic et al. [15] evaluated entropy generation in an enlarged tube using different hybrid nanofluids and found that MWCNT + Fe_3O_4 combinations outperformed other configurations in both heat transfer and entropy reduction. Shahsavar et al. [**?**] optimized entropy and heat transfer performance of non-Newtonian hybrid nanofluids in a concentric annulus, demonstrating their suitability in confined geometries. Tong et al. [36] used MWCNT-enhanced Fe_3O_4 nanofluids to improve photo-thermal conversion and solar absorption. Boroomandpour et al. [8] estimated the thermal conductivity of ternary nanofluids (MWCNT + TiO_2+ ZnO), further emphasizing the customizability of hybrid nanofluids for solar systems. Abbas et al. [1] studied a Ti_2/Fe_2O_3-water hybrid nanofluid in automobile radiators and reported a 26.7% increase in heat transfer. However, they noted that exceeding 0.009 vol% nanoparticle concentration led to clogging and reduced system stability. Shoaib et al. [35] examined 3D MHD flow near a rotating disk and included thermal radiation, ohmic heating, and viscous dissipation, showcasing the practical complexity that hybrid nanofluids can accommodate. Zada et al. [42] analyze the water and ethylene glycol (50%W + 50% EG) based hybrid nanofluid confined between parallel disk by incorporating nanotubes via homotopy analysis method. Bashirnezhad et al. [7] experimentally optimized a solar flat plate collector system using perforated twisted tape turbulators and a CuO-MWCNT hybrid nanofluid, concluding that hybid nanofluid significantly improves heat transfer efficiency (over 67%) and reduces energy cost to 0.024 USD/kWh.

The interaction between motile micro-organisms and nanoparticles within fluid flows plays a crucial role in convective heat and mass transfer. Micro-organisms are often categorized as oxytactic, chemotactic, or gyrotactic, while nanoparticles exhibit non-motile behavior driven by Brownian motion and thermophoresis. Kuznetsov and Avramenko [20] pioneered the concept of bioconvection due to gyrotactic micro-organisms in a finite-depth fluid domain. Subsequent research has expanded this framework. Rana et al. [27] employed the shooting method to numerically examine the swimming behavior of gyrotactic microorganisms in a Jeffrey fluid near a stretching surface, concluding that Brownian motion leads to a reduction in microorganism concentration. Rao et al. [28] used the bvp4c solver and observed that an increase in the bioconvection Lewis number diminishes the density of motile microorganisms near a vertical surface. He et al. [14] reported that the buoyancy effects induced by both microbes and nanoparticles cause a decay in flow velocity in an MHD Carreau nanofluid. Furthermore, Hussain et al. [**?**] found that lower values of the bioconvection Lewis number lead to a thinner concentration boundary layer around a time-dependent, rotating, stretchable disk, resulting in faster thermal energy dissipation from the system.

The aerospace industry is actively exploring solar energy as a sustainable alternative to fossil fuels. Historical milestones include the creation of the first solar-powered aircraft, AstroFlight Sunrise in 1973, followed by the Mauro Solar Riser in 1979, which became the first piloted solar aircraft. These early ventures laid the foundation for the modern-day Solar Impulse 2, which in 2016 successfully

completed a solar-powered circumnavigation of the globe, setting 19 aviation records including a 118-hour continuous flight [10] as illustrated in Figure 1. Gao et al. [12] recommended control strategies utilizing gravitational potential energy to maximize energy efficiency. Barbosa et al. [**?**] proposed a solar aircraft with a hydrogen energy storage system and identified tools to prevent over- or under-sizing of power units. These achievements brought mainstream attention to solar-powered flight and sparked renewed scientific interest. The transportation sector, responsible for 27% of global greenhouse gas emissions [17], is now increasingly targeted for decarbonization via renewable aviation technologies. Wu et al. contributed multiple design studies addressing endurance improvement through Z-shaped wing geometry [38], wingtip connection optimization [39], and rotatable V-shaped wing architecture [40]. To enhance flight efficiency, Wang et al. [**?**] implemented the Gauss pseudo-spectral method for flight path optimization. Collectively, these studies reflect the field's progression from conceptual validation to system optimization.

FIGURE 1. systematic representation of physical model.

A persistent challenge in solar aircraft design is ensuring uninterrupted flight across day–night cycles. Solar aircraft must harvest energy during daylight and store sufficient reserves for night operations. Gao et al. [13] provided a critical review of current techniques for solar energy harvesting and storage, highlighting thermal management as a bottleneck. Maleki et al. [22] emphasized that nanofluids improve collector thermal efficiency. Kashyap et al. [18] explored entropy generation using the same hybrid nanofluid under various boundary conditions, while Khosravi et al. [19] used artificial neural networks to predict entropy behavior in microchannel flows. These efforts suggest that hybrid nanofluids not only enhance heat absorption but also regulate energy dissipation, two critical factors for extending solar aircraft performance into the night. Armaghani et al. [5] addressed entropy generation in MHD mixed convection of Al_2O_3-Cu/water hybrid nanofluids in an L-shaped enclosure, confirming improved thermodynamic efficiency. Shamshuddin et al. [29] demonstrated how nanofluid properties could be

fine-tuned for optical control in solar absorption. However, the complexity of thermal regulation under varying solar intensities called for more advanced solutions of hybrid nanofluids.

This concept is physically realized in the structure shown in Figure 2, which depicts a parabolic trough solar collector (PTSC) embedded within a solar aircraft wing. This trough collects solar radiation during flight, ensuring a continuous energy supply. The inclusion of hybrid nanofluids in this collector significantly improves heat retention, especially when the aircraft encounters lower solar intensity or moves into nighttime flight. Thus, hybrid nanofluids not only improve thermal conductivity but also contribute to entropy regulation, energy storage, and thermal resilience all critical for enabling solar-powered aircraft to operate over full diurnal cycles.

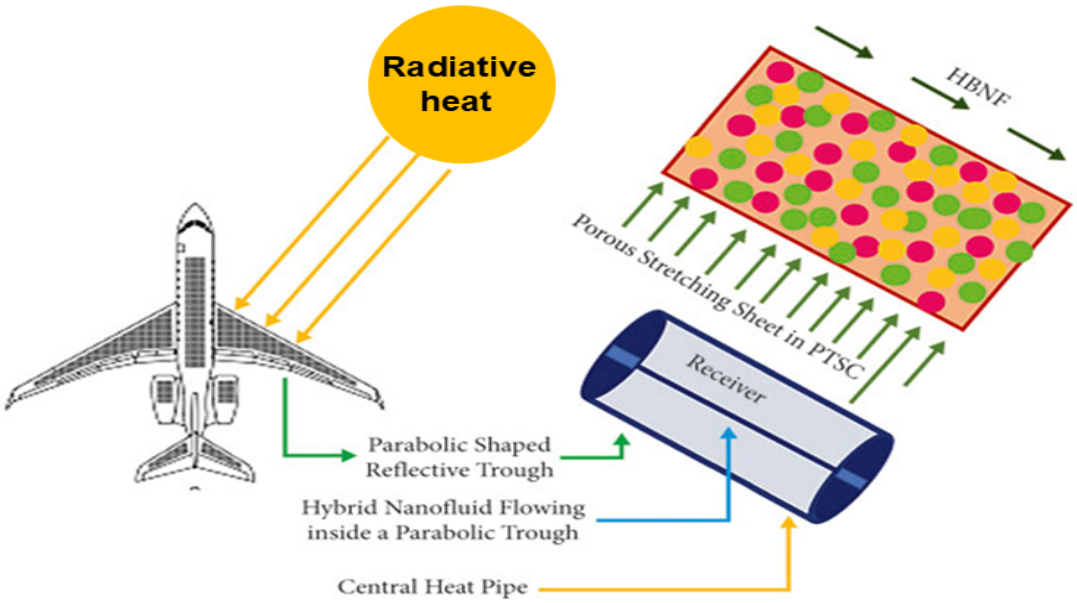

FIGURE 2. systematic representation of physical model.

Minimizing entropy generation is essential for improving the performance and sustainability of thermal and fluid systems. Since it directly measures irreversibility, lower entropy generation translates into better energy utilization, reduced exergy destruction, and higher overall efficiency. This has significant implications in engineering fields such as power generation, refrigeration, chemical processing, and heat exchangers, where minimizing energy losses is crucial for cost-effectiveness and sustainability [6]. Several recent studies have explored entropy generation in different fluid and thermal systems. Shahzad et al. [31] reported that entropy generation intensifies with increasing Reynolds number in SWCNT-MWCNT/kerosene oil hybrid nanofluid flow, analyzed using the Keller box scheme. Pattnaik et al. [25] demonstrated that Carreau ternary hybrid nanofluids enhance thermal conductivity, thereby improving temperature regulation in solar aircraft. Ogunsanwo et al. [24] highlighted that the Williamson parameter significantly increases the thermal response of $Cu\text{-}TiO_2/EG$ hybrid nanofluid. Likewise, Majumder et al. [23] showed that adjusting the volume fraction of carbon nanotubes reduces thermal irreversibility in flows over a rotating sphere, with solutions obtained using the bvp4c solver.

To the best of the authors' knowledge, no prior research has undertaken a comparative analysis of mono nanofluid and hybrid nanofluid based on sodium alginate (SA) within the framework of a bio-convective Williamson fluid model, incorporating a velocity slip condition and convective boundary constraints over a chemically reactive stretching sheet in a solar-energy-inspired configuration. This study fills that gap by systematically evaluating how inclined magnetic fields and nonlinear radiative heat flux influence the rates of heat and mass transfer in both nanofluid types. Furthermore, entropy generation analysis is performed to assess thermodynamic irreversibilities in the system. The governing equations are transformed into a system of ordinary differential equations using similarity variables and numerical solutions are obtained using the shooting method. Detailed graphical and tabular results are presented to highlight how slip effects, solar-induced thermal radiation, and chemical reactions impact the flow and transport characteristics.

Motivated by the above novelty, this study addresses the following key questions:

- How do inclined magnetic fields influence heat transfer rate, skin friction coefficient, and flow resistance in SA-based nanofluids?
- In what way does nonlinear thermal radiation affect entropy generation and thermodynamic irreversibility?
- How does velocity slip at the boundary alter the fluid velocity distribution and transport processes?
- What role do chemical reactions play in modifying concentration profiles of mono nanofluids versus hybrid nanofluids?
- Which fluid, mono nanofluid or hybrid nanofluid, demonstrates better heat transfer efficiency and thermal conductivity under solar-inspired conditions?

  How do convective boundary constraints regulate the rate of heat transfer in both fluid models?

2. Formulations for the Flow Model

This study investigates the unsteady, two-dimensional, laminar bioconvective Williamson hybrid nanofluid flow over a chemically reactive, horizontally stretching surface exposed to thermal radiation, internal heat generation, and viscous dissipation effects. The surface is stretched along the x-axis with a stretching velocity U_w, while an inclined magnetic field of strength B is applied at an angle Υ to the surface. The hybrid nanofluid comprises sodium alginate (SA) as the base fluid, enhanced with graphene oxide (GO) and copper (Cu) nanoparticles. Additional physical effects include chemical reaction, magnetohydrodynamics, and bioconvection of motile microorganisms. The surface temperature and stretching velocity vary in both space and time, and are formulated as follows [3, 33]:

$$T_w(x,t) = T_\infty + \frac{b^* x}{1-\xi t},\ U_w(x,t) = \frac{bx}{1-\xi t}. \tag{2.1}$$

The Williamson fluid model is adopted to capture non-Newtonian rheology. The Cauchy stress tensor S^* is expressed as:

$$S^* = \tau_{ij} - pI, \tag{2.2}$$

where p describe the pressure, I is the identity tensor. The latter is defined by the Williamson model as:

$$\tau_{ij} = \left[\mu_\infty + \frac{(\mu_0 - \mu_\infty)}{(1-\zeta\gamma)}\right] A_\beta, \tag{2.3}$$

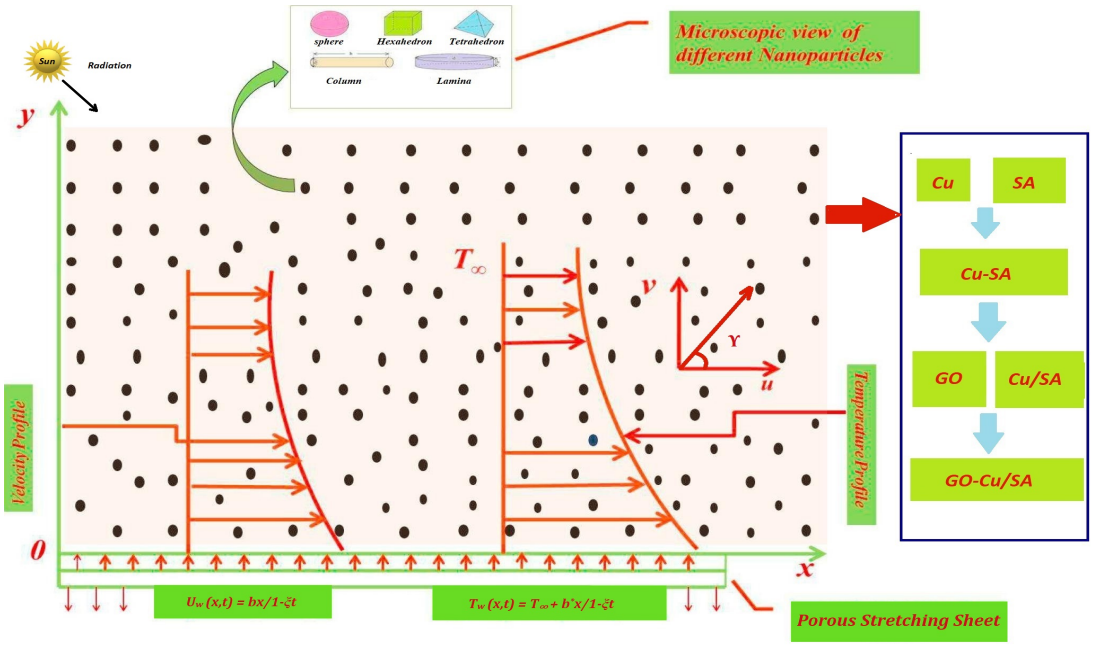

FIGURE 3. systematic representation of physical model.

where μ_∞ and μ_0 represent the infinite and zero shear-rate viscosities, respectively, ζ is the Williamson parameter, and A_β is the first Rivlin-Ericksen tensor. The magnitude of the shear rate γ is defined as:

$$\gamma = \sqrt{\frac{1}{2}\pi} \textbf{ with } \pi = trace(A_\beta^2).$$

Assuming $\mu_\infty = 0$ and $\zeta\gamma < 1$, the stress tensor simplifies to:

$$\tau_{ij} = \left[\frac{\mu_0}{(1-\zeta\gamma)}\right] A_\beta. \tag{2.4}$$

Applying the binomial expansion for small $\zeta\gamma$, we obtain:

$$\tau_{ij} \approx [\mu_0(1+\zeta\gamma)] A_\beta. \tag{2.5}$$

The flow model's geometry inside the (PTSC) is depicted in Fig. 3 as: Taking into account the effects of an inclined magnetic field, porous media resistance modeled through the Darcy–Forchheimer formulation, thermal radiation, viscous dissipation, chemical reaction and bioconvection, the complete set of governing equations for continuity, momentum, thermal, concentration, and motile microorganism

density are formulated as follows [30, 21]:

$$\frac{\partial G_1}{\partial x}+\frac{\partial G_2}{\partial y}=0, \tag{2.6}$$

$$\frac{\partial G_1}{\partial t}+G_1\frac{\partial G_1}{\partial x}+G_2\frac{\partial G_2}{\partial y}=\frac{\mu_{hnf}}{\rho_{hnf}}\frac{\partial^2 G_1}{\partial y^2}+\sqrt{2}\zeta\frac{\mu_{hnf}}{\rho_{hnf}}\Big[\frac{\partial G_1}{\partial y}\frac{\partial^2 G_1}{\partial y^2}\Big]-\frac{\mu_{hnf}}{\rho_{hnf}k}G_1$$
$$-\frac{\sigma_{hnf}}{\rho_{hnf}}B^2G_1Sin^2(\Upsilon), \tag{2.7}$$

$$\frac{\partial T}{\partial t}+G_1\frac{\partial T}{\partial x}+G_2\frac{\partial T}{\partial y}=\frac{\kappa_{hnf}}{(\rho C_p)_{hnf}}\Big[\frac{\partial^2 T}{\partial y^2}\Big]-\frac{1}{(\rho C_p)_{hnf}}\Big[\frac{\partial q_r}{\partial y}\Big]+\frac{\mu_{hnf}}{(\rho C_p)_{hnf}}\Big[\frac{\partial G_1}{\partial y}\Big]^2$$
$$+\frac{Q_0}{(\rho C_p)_{hnf}}(T-T_\infty)+\frac{\sigma_{hnf}}{\rho_{hnf}}B^2G_1Sin^2(\Upsilon), \tag{2.8}$$

$$\frac{\partial C}{\partial t}+G_1\frac{\partial C}{\partial x}+G_2\frac{\partial C}{\partial y}=D_{hnf}\frac{\partial^2 C}{\partial y^2}-k_1(C-C_\infty), \tag{2.9}$$

$$\frac{\partial N}{\partial t}+G_1\frac{\partial N}{\partial x}+G_2\frac{\partial N}{\partial y}=D_m\frac{\partial^2 N}{\partial y^2}+\frac{bWc}{C_w-C_\infty}\frac{\partial}{\partial y}\big(N\frac{\partial C}{\partial y}\big), \tag{2.10}$$

The associated boundary conditions are specified as [**?**]:

$$\left.\begin{aligned} &G_1(x,0)=U_w+N_w\left\{1+\zeta\Big(\frac{\partial G_1}{\partial y}\Big)\right\}\frac{\partial G_1}{\partial y},\ G_2(x,0)=V_w,\\ &-k_0\Big(\frac{\partial T}{\partial y}\Big)=h_f(T_w-T),\ C=C_w,\ N=N_w\ at\ y=0,\\ &G_1\to 0,\ C\to C_\infty,\ T\to T_\infty,\ N\to N_\infty,\ as\ y\to\infty. \end{aligned}\right\} \tag{2.11}$$

The fluid velocity, represented in vector form as $\vec{G}=[G1(x,y,t),G2(x,y,t),0]$, where t denotes time, T represents the fluid's temperature, "N_w" signifies the slip length, T_w denotes the temperature of the surrounding plate, and h_f indicates the Convective heat transfer coefficient.

The radiative heat flux is defined as[33]:

$$q_r=-\frac{4\sigma^*}{3k^*}\frac{\partial T^4}{\partial y}, \tag{2.12}$$

where σ^* represents the Stefan-Boltzmann constant, and k^* is the absorption coefficient. If the temperature difference is sufficiently small, the temperature T^4 can be approximated by expanding it about T_∞ using a Taylor series, as shown below:

$$T^4=T_\infty^4+4T_\infty^3(T-T_\infty)+6T_\infty^2(T-T_\infty)^2+...$$

2.1. **Formulation of thermo-physical properties.** The effective thermo-physical properties of the hybrid nanofluid `GO-Cu/SA`, formed by dispersing graphene oxide `(GO)` and copper `(Cu)` nanoparticles in sodium alginate (SA), are summarized in Table 1. The formulations of various thermo-physical properties for the hybrid nanofluid are illustrated in Table 2.

TABLE 1. Thermo-physical properties of hybrid naonofluid [**?**]

Feature	Hybrid nanofluid GO-Cu/SA
Viscosity (ν)	$\mu_{hnf} = \mu_f(1-\phi_{\mathtt{Cu}})^{-2.5}(1-\phi_{\mathtt{GO}})^{-2.5}$
Heat Capacity (ρC_p)	$(\rho C_p)_{hnf} = (1-\phi_{\mathtt{GO}})[(1-\phi_{\mathtt{Cu}})(\rho C_p)_f + \phi_{\mathtt{Cu}}(\rho C_p)_{\mathtt{Cu}}] + \phi_{\mathtt{GO}}(\rho C_p)_{\mathtt{GO}}$
Thermal conductivity (κ)	$\frac{\kappa_{hnf}}{\kappa_{nf}} = \left[\frac{\kappa_{\mathtt{GO}}+(r-1)\kappa_{nf}-(r-1)\phi_{\mathtt{GO}}(\kappa_{nf}-\kappa_{\mathtt{GO}})}{\kappa_{\mathtt{GO}}+(r-1)\kappa_{nf}+\phi_{\mathtt{GO}}(\kappa_{nf}-\kappa_{\mathtt{GO}})}\right]$, $\frac{\kappa_{nf}}{\kappa_f} = \left[\frac{\kappa_{\mathtt{Cu}}+(r-1)\kappa_f-(r-1)\phi_{\mathtt{Cu}}(\kappa_f-\kappa_{\mathtt{Cu}})}{\kappa_{\mathtt{Cu}}+(r-1)\kappa_f+\phi_{\mathtt{Cu}}(\kappa_f-\kappa_{\mathtt{Cu}})}\right]$
Electrical conductivity (σ)	$\frac{\sigma_{hnf}}{\sigma_f} = \left[1+\frac{3(\frac{\phi_{\mathtt{Cu}}\sigma_{\mathtt{Cu}}+\phi_{\mathtt{GO}}\sigma_{\mathtt{GO}}}{\sigma_f}-(\phi_{\mathtt{Cu}}+\phi_{\mathtt{GO}}))}{(\frac{\phi_{\mathtt{Cu}}\sigma_{\mathtt{Cu}}+\phi_{\mathtt{GO}}\sigma_{\mathtt{GO}}}{(\phi_{\mathtt{Cu}}+\phi_{\mathtt{GO}})\sigma_f}+2)-(\frac{\phi_{\mathtt{Cu}}\sigma_{\mathtt{Cu}}+\phi_{\mathtt{GO}}\sigma_{\mathtt{GO}}}{\sigma_f}-(\phi_{\mathtt{Cu}}+\phi_{\mathtt{GO}}))}\right]$
Density (ρ)	$\rho_{hnf} = (1-\phi_{\mathtt{GO}})\big((1-\phi_{\mathtt{Cu}})\rho_f + \phi_{\mathtt{Cu}}\rho_{\mathtt{Cu}}\big) + \phi_{\mathtt{GO}}\rho_{\mathtt{GO}}$

TABLE 2. Thermo-physical properties of fluid and nanoparticles.

Physical properties	ρ(kg/m^3)	C_p (J/kg K)	k (W/m K)	σ (S/m)
Sodium alginate SA	989	4175	0.6376	2.6×10^{-4}
Copper Cu	8933	385	401	5.96×10^{7}
Graphene oxide GO	1800	717	5000	1.1×10^{-5}

2.2. **Non-dimensionalization of governing model.** To transform the mathematical model from partial differential equations (2.6)-(2.10) into ordinary differential equations (ODEs), the following similarity transformation, as described in reference, is employed [4]:

$$\left.\begin{aligned} &\eta(x,y) = \sqrt{\frac{b}{\nu_f(1-\xi t)}}y,\ \ \Phi(\eta) = \frac{C-C_\infty}{C_w-C_\infty}, \\ &\theta(\eta) = \frac{T-T_\infty}{T_w-T_\infty},\ \ \psi(x,y) = \sqrt{\frac{\nu_f b}{(1-\xi t)}}xf(\eta),\ \ \chi(\eta) = \frac{N-N_\infty}{N_w-N_\infty}. \end{aligned}\right\} \tag{2.13}$$

Here, "ψ" represents the stream function, and "η" is the similarity variable. By utilizing the stream function, the velocity components are expressed as

$$G_1 = \frac{\partial\psi}{\partial y},\ \ G_2 = -\frac{\partial\psi}{\partial x}. \tag{2.14}$$

By using the transformation (2.13), equation (2.6) is inherently satisfied, and the remaining equations (2.7)–(2.10) take the following dimensionless form:

$$f''' + N_aN_b\Big(ff'' - f'^2 - A\Big(f' + \frac{\eta}{2}f''\Big) - \frac{N_e}{N_b}MSin^2(\Upsilon)f'\Big) + \lambda f''f''' - Kf' = 0, \tag{2.15}$$

$$\left(1+\frac{PrNr}{N_d}\right)\theta'' + \frac{PrN_c}{N_d}\left(f\theta' - f'\theta - A\Big(\theta+\frac{\eta}{2}\theta'\Big) + \frac{Ec(f'')^2}{N_aN_c} + \frac{Q\theta}{N_c} + \frac{N_e}{N_c}EcMf'^2Sin^2(\Upsilon)\right) = 0, \tag{2.16}$$

$$\Phi'' + \frac{Sc}{N_a}\left(f\Phi' - A\frac{\eta}{2}\Phi' - K_1\Phi\right) = 0, \tag{2.17}$$

$$\chi'' - Lb\left(\frac{A}{2}x - f\right)\chi' + Pe\Big((\varpi+\chi)\Phi'' + \Phi'\chi'\Big) = 0. \tag{2.18}$$

The transformed boundary conditions are as follows:

$$\left.\begin{aligned} &f(0) = S,\ f'(0) = 1 + \Lambda\left(f''(0) + \frac{\lambda}{2}(f''(0))^2\right),\\ &\theta'(0) = -Bi(1-\theta(0)),\ \Phi(0) = 1,\ \chi(0) = 1.\\ &f' \to 0,\ \theta \to 0,\ \Phi \to 0,\ \chi \to 0\ \eta \to \infty. \end{aligned}\right\} \tag{2.19}$$

In the equations provided above, the various parameters used have the following definitions:

$$N_a = (1-\phi_{\mathtt{Cu}})^{2.5}(1-\phi_{\mathtt{GO}})^{2.5}, \tag{2.20}$$

$$N_b = (1-\phi_{\mathtt{GO}})\left((1-\phi_{\mathtt{Cu}}) + \phi_{\mathtt{Cu}}\frac{\rho_{\mathtt{Cu}}}{\rho_f}\right) + \phi_{\mathtt{GO}}\frac{\rho_{\mathtt{GO}}}{\rho_f}, \tag{2.21}$$

$$N_c = (1-\phi_{\mathtt{GO}})\left((1-\phi_{\mathtt{Cu}}) + \phi_{\mathtt{Cu}}\frac{(\rho C_p)_{\mathtt{Cu}}}{(\rho C_p)_f}\right) + \phi_{\mathtt{GO}}\frac{(\rho C_p)_{\mathtt{GO}}}{(\rho C_p)_f}, \tag{2.22}$$

$$N_d = \left[\frac{\kappa_{\mathtt{GO}} + 2\kappa_{nf} - 2\phi_{\mathtt{GO}}(\kappa_{nf} - \kappa_{\mathtt{GO}})}{\kappa_{\mathtt{GO}} + 2\kappa_{nf} + \phi_{\mathtt{GO}}(\kappa_{nf} - \kappa_{\mathtt{GO}})}\right] \times \left[\frac{\kappa_{\mathtt{Cu}} + 2\kappa_f - 2\phi_{\mathtt{Cu}}(\kappa_{1f} - \kappa_{\mathtt{Cu}})}{\kappa_{\mathtt{Cu}} + 2\kappa_{1f} + \phi_{\mathtt{Cu}}(\kappa_f - \kappa_{\mathtt{Cu}})}\right], \tag{2.23}$$

$$N_e = \left[1 + \frac{3(\frac{\phi_{\mathtt{Cu}}\sigma_{\mathtt{Cu}} + \phi_{\mathtt{GO}}\sigma_{\mathtt{GO}}}{\sigma_f} - (\phi_{\mathtt{Cu}} + \phi_{\mathtt{GO}}))}{(\frac{\phi_{\mathtt{Cu}}\sigma_{\mathtt{Cu}} + \phi_{\mathtt{GO}}\sigma_{\mathtt{GO}}}{(\phi_{\mathtt{Cu}} + \phi_{\mathtt{GO}})\sigma_f} + 2) - (\frac{\phi_{\mathtt{Cu}}\sigma_{\mathtt{Cu}} + \phi_{\mathtt{GO}}\sigma_{\mathtt{GO}}}{\sigma_f} - (\phi_{\mathtt{Cu}} + \phi_{\mathtt{GO}}))}\right]. \tag{2.24}$$

Here $S = -V_w\sqrt{(1-\xi t)/nu_f b}$ is the suction/injection parameter, $\Lambda = \sqrt{b/\nu_f(1-\xi t)}\,N_w$ is the velocity slip parameter and $B_i = \frac{h_f}{k_0}\sqrt{\nu_f(1-\xi)t/b}$ is the Biot number.

Different dimensionless parameters are formulated as:

$$A = \frac{\xi}{b},\ \lambda = U_w\sqrt{\frac{2b}{\mu_f(1-\xi t)}},\ M = \frac{\sigma_f B_0^2}{b\rho_f},\ K = \frac{\nu_f(1-\xi t)}{bk},\ \alpha_f = \frac{\kappa_f}{(\rho C_p)_f},\ Pr = \frac{\nu_f}{\alpha_f}$$

$$Ec = \frac{U_w^3}{(C_p)_f(T_w - T_\infty)},\ Bi = \frac{h_f}{k_0}\sqrt{\frac{\nu_f(1-\xi t)}{b}},\ Nr = \frac{16\sigma^*}{3\kappa^*}\frac{T_\infty^3}{\nu_f(\rho C_p)_f},\ Q = \frac{Q_0 x}{(\rho C_p)_f U w},$$

$$Sc = \frac{\nu_f}{D_f},\ K_1 = \frac{k_1(1-\xi t)}{b},\ Lb = \frac{\nu_f}{Dm},\ Pe = \frac{bWc}{Dm},\ \varpi = \frac{N_\infty}{N_w - N_\infty}.$$

2.3. **Physical quantities for engineering interest.** The essential physical parameters of interest, including the skin friction coefficient, motile density number, local Nusselt number and local Sherwood number are defined as [32, 41]:

$$C_f = \frac{\tau_w}{\rho_f U_w^2},\ Sn_x = -\frac{xq_m}{D_{hnf}(N_w - N_\infty)},\ Nu_x = \frac{xq_w}{\kappa_f(T_w - T_\infty)},\ Sh_x = \frac{xq_m}{D_{hnf}(C_w - C_\infty)}, \tag{2.25}$$

where τ_w represents the skin friction or shear stress, q_w is the wall heat flux from the plate, q_m denotes the concentration flux from the surface and q_m is expressed as:

$$\tau_w = \mu_{hnf}\left(\frac{\partial G_1}{\partial y} - \frac{\zeta}{\sqrt{2}}\Big(\frac{\partial G_1}{\partial y}\Big)^2\right)\Bigg|_{\text{at } y=0},\ q_w = -\kappa_{hnf}\left\{1 + \frac{16\sigma^* T_\infty^3}{3k^*\nu_f(\rho C_p)_f}\right\}\frac{\partial T}{\partial y}\Bigg|_{\text{at } y=0},$$

$$q_m = -D_{hnf}\,\frac{\partial C}{\partial y}\Bigg|_{\text{at } y=0},\ q_m = -D_{hnf}\,\frac{\partial N}{\partial y}\Bigg|_{\text{at } y=0}.$$

Dimensionless forms of skin friction, Nusselt, Sherwood and motile density numbers are:

$$C_f Re_x^{\frac{1}{2}} = \frac{f''(0)}{N_a}\left(1+\frac{\lambda}{2}f''(0)\right),$$
$$Nu_x Re_x^{-\frac{1}{2}} = -\frac{\kappa_{hnf}}{\kappa_f}(1+Nr)\theta'(0),\ Sh_x Re_x^{\frac{1}{2}} = -\Phi'(0),\ Sn_x Re_x^{-\frac{1}{2}} = -\chi'(0).$$

2.4. **Entropy generation.** Entropy generation serves as a key indicator of irreversibility in thermodynamic systems. According to the second law of thermodynamics, any real process is accompanied by entropy production, which corresponds to the loss of useful energy. In heat and fluid flow systems, entropy is generated due to temperature gradients, viscous effects, magnetic field interactions (Joule heating), and molecular diffusion. The evaluation of entropy generation is particularly essential in high-performance applications such as solar-powered aircraft, where energy conservation and thermal efficiency are critical. A comprehensive understanding of entropy behavior allows engineers to optimize system design by reducing energy losses and improving performance.

In this study, entropy generation is evaluated by considering contributions from thermal conduction, radiative heat transfer, viscous dissipation, and Joule heating effects. The dimensional form of the local volumetric entropy generation rate is given as [32]:

$$E_G = \frac{\kappa_{hnf}}{T_\infty^2}\left(\left(\frac{\partial T}{\partial y}\right)^2 + \frac{16}{3}\frac{16\sigma^* T_\infty^3}{3k^*\nu_f(\rho C_p)_f}\left(\frac{\partial T}{\partial y}\right)^2\right) + \frac{\mu_{hnf}}{T_\infty}\left(\frac{\partial G_1}{\partial y}\right)^2 + \frac{\mu_{hnf}G_1^2}{kT_\infty}. \tag{2.26}$$

To make this expression dimensionless, the entropy generation number N_g is introduced as:

$$N_g = \frac{T_\infty^2 b^2 E_G}{\kappa_f (T_w - T_\infty)^2}, \tag{2.27}$$

where k_f is the thermal conductivity of the base fluid, T_w is the wall temperature, and b is the stretching rate. Using appropriate similarity variables, the final non-dimensional form of entropy number is obtained:

$$N_g = N_d(1+Nr)Re\theta'^2 + \frac{Br}{N_a}\frac{Re}{\Omega}(Kf'^2 + f''^2). \tag{2.28}$$

Here, Re represents the Reynolds number as $\frac{U_w b^2}{\nu_f x}$ and Br is the Brinkmann number given by $\frac{\mu_f U_w^2}{\kappa_f(T_w - T_\infty)}$.

3. Solution methodology

The system of nonlinear ordinary differential equations (2.10)-(2.13) along with the boundary conditions (2.14) is solved numerically using the shooting method based on the Runge–Kutta fourth-order method and Newton's method [9]. The equation (2.10) will be transformed into a system of first-order differential equations by using the following notations:

$$f = \zeta_1, f' = \zeta_1' = \zeta_2, f'' = \zeta_2' = \zeta_3. \tag{3.1}$$

As a consequence of the above notations, the following system of ODEs is obtained:

$$\left.\begin{aligned}
\zeta_1' &= \zeta 2,\\
\zeta_2' &= \zeta 3,\\
\zeta_3' &= \frac{-1}{1+\lambda\zeta_3}\left[N_a N_b\left\{\zeta_1\zeta_3 - \zeta_2^2 - A\left(\zeta_2 + \frac{\eta}{2}\zeta_3\right) - \frac{N_e}{N_b}M\sin^2(\gamma)\zeta_2\right\} - K\zeta_2\right],
\end{aligned}\right\} \tag{3.2}$$

with

$$\zeta 1(0) = S,\ \zeta 2(0) = 1 + \Lambda\left\{\zeta_3(0) + \frac{\lambda}{2}\zeta_3(0)^2\right\},\ \zeta_3(0) = \tau_1, \tag{3.3}$$

where τ_1 is the missing initial condition. The above initial value problem is solved numerically by RK-4 method. The missing conditions τ_1 is assumed to satisfy the following relation:

$$\zeta 2(\eta_\infty, \tau_1) = 0.$$

The Newton's method will be used to find τ_l. This method has the following iterative scheme:

$$\tau_1^{n+1} = \tau_1^n - \frac{\zeta_2\left(\eta_\infty, \tau_1^n\right)}{\left(\frac{\partial}{\partial \tau_1}\zeta_2\left(\eta_\infty, \tau_1\right)\right)^n}. \tag{3.4}$$

We further introduce the following notation:

$$\frac{\partial \zeta_1}{\partial \tau_1} = \zeta_4, \ \frac{\partial \zeta_2}{\partial \tau_1} = \zeta_5, \ \frac{\partial \zeta_3}{\partial \tau_1} = \zeta_6. \tag{3.5}$$

As a result of these new notations, Newton's iterative scheme takes the following form:

$$\tau_1^{n+1} = \tau_1^n - \frac{\zeta_2\left(\eta_\infty, \tau_1^n\right)}{\left(\frac{\partial}{\partial \tau_1}\zeta_2\left(\eta_\infty, \tau_1\right)\right)^n}. \tag{3.6}$$

Now differentiating the most recently presented system of three first order ODEs with respect to τ_1, we get another system of ODEs, as follows:

$$\left.\begin{aligned} \zeta_4' &= \zeta 5, \\ \zeta_5' &= \zeta 6, \\ \zeta_6' &= -\frac{N_a N_b\left\{\zeta_1\zeta_6 + \zeta_3\zeta_4 - \zeta_2\zeta_4 - A\left(\zeta_4 + \frac{\eta}{2}\zeta_6\right) - \frac{N_e}{N_b}M\sin^2(\gamma)\zeta_4 - K\zeta_4\right\}}{(1+\lambda\zeta_3)} - \frac{\lambda\zeta_6}{(1+\lambda\zeta_3)}\zeta_3' \end{aligned}\right\} \tag{3.7}$$

with

$$\zeta_4 = 0, \ \zeta_5 = \Lambda\left\{1 + \lambda\tau_1\right\}, \ \zeta_6 = 0. \tag{3.8}$$

The stopping criterion for Newton's method is defined as

$$\left|\widetilde{X}_2\left(\zeta_\infty, \tau_1\right)\right| < \epsilon,$$

for an arbitrarily small positive value ϵ. In this study, ϵ is taken as 10^{-10}. Equations (2.16)–(2.18) are solved simultaneously using the same procedure [33].

4. Validation

To ensure the accuracy of the numerical approach, the current results were compared with existing literature data [16, 4]. The observed agreement, presented in Table 3, confirms the validity of the computational model.

Table 3. Compression of present finding of $-f''(0)$ against parameter M when other parameters are zero.

M	[16]	[4]	Present
0.0	1.000000	1.000008	1.00048
0.2	1.095445	1.095446	1.0955600
0.5	1.224745	1.224745	1.229776
1	1.414214	1.414213	1.414216
1.2	1.483240	1.483239	1.483241

5. Results and Discussions

This section comprehensively analyzes the influence of several key dimensionless parameters on nanofluid and hybrid fluid flow behavior and entropy generation using graphical representations. Furthermore, the effects on heat and mass transfer rates, drag force, and motile microorganism density are presented through both tables and graphs.

5.1. **Computational results.** In this section, the effects of several parameters on different physical quantities are described using Table 4–5 and Figures 4–5. Suction enhances boundary layer thinning, which leads to an increase in skin friction. For the nanofluid, the skin friction coefficient increases by up to 4.05%, while for the hybrid nanofluid, the change is slightly lower at 3.62%, as illustrated in Table 4. The introduction of a magnetic field contributes to an opposing Lorentz force, increasing flow resistance and thereby skin friction. The corresponding changes are 2.45% for the nanofluid and 3.01% for the hybrid nanofluid, indicating that hybrid nanoparticles slightly intensify magnetic drag effects due to their stronger interaction with the applied field. Table 5 and Figure 5 illustrate the influence of various parameters on the Nusselt number, a measure of the heat transfer rate. The hybrid nanofluid consistently demonstrates superior thermal performance compared to the mono nanofluid. Overall, the heat transfer rate increases by 14.90% in the nanofluid and by 15.20% in the hybrid nanofluid, confirming the thermal advantage of GO–Cu hybrid dispersions.

A remarkable sensitivity is observed with the Biot number (Bi), which governs the internal thermal resistance of the sheet surface. The heat transfer rate varies significantly from 40.60% to 86.54% in the nanofluid, and 39.90% to 85.67% in the hybrid nanofluid, highlighting the importance of thermal boundary resistance in systems such as solar aircraft wing collectors, where surface heating and convection dominate the thermal exchange.

Moreover, the radiation parameter (N_r), as shown in Figure 5, positively affects the rate of heat transfer. An increase in N_r enhances thermal radiation emission from the surface, which is crucial for solar energy absorption in high-altitude flights where direct solar flux is more intense. The hybrid nanofluid shows improved thermal reactivity under radiation, attributed to the high conductivity and specific heat of GO nanoparticles. The chemical reaction parameter (K_r) influences the Sherwood number, representing the mass transfer rate. Table 5 confirms that chemical reactivity enhances mass transport for both fluid types. For the nanofluid, the mass transfer rate improves by 21.53%, while the hybrid nanofluid shows a rise of 16.40%. Although the hybrid nanofluid performs slightly lower in mass transfer enhancement, it compensates with better thermal and entropy performance. This behavior is particularly important in airborne catalytic and combustion processes in aircraft propulsion and energy systems.

5.2. **Velocity field.** Figure 6 presents the influence of the porosity parameter K on the velocity distribution for both nanofluid and hybrid nanofluid configurations. As the value of K increases, the porous medium imposes greater resistance to the fluid motion due to enhanced drag within the medium's structure. Physically, a higher porosity parameter indicates denser packing of the porous matrix, which hinders fluid penetration and dissipates kinetic energy through internal friction. This resistance suppresses momentum transport, resulting in a noticeable reduction in fluid velocity across the boundary layer. The hybrid nanofluid `GO-Cu/SA` retains a comparatively thicker boundary layer and slightly higher velocity than its monofluid counterpart, owing to the synergistic effect of graphene oxide and copper nanoparticles, which improve fluid mobility by enhancing effective viscosity and reducing the resistance of flow through pores. This reflects its superior flow resilience in porous environments, a feature particularly valuable in filtration and catalytic processes where porous media are common.

]

TABLE 4. Results of $Re_x^{\frac{1}{2}} C_f$ and $Re_x^{\frac{-1}{2}} N_u$.

λ	S	K	A	Λ	Υ	M	Ec	Nr	Bi	Q	$Re_x^{\frac{1}{2}} C_f$ Cu-SA	$Re_x^{\frac{1}{2}} C_f$ GO-Cu/SA	$Re_x^{\frac{1}{2}} Nu_x$ Cu-SA	$Re_x^{\frac{1}{2}} Nu_x$ GO-Cu/SA
0.1	0.1	0.1	0.1	0.3	$\pi/2$	0.1	0.2	0.3	0.2	0.1	-1.1112	-1.3124	0.2606	0.3266
0.2											-1.0986	-1.2982	0.2592	0.3247
0.3											-1.0846	-1.2825	0.2576	0.3225
	0.2										-1.1562	-1.3599	0.2641	0.3312
	0.3										-1.2025	-1.4086	0.2676	0.3356
		0.3									-1.1626	-1.3868	0.2572	0.3206
		0.4									-1.1854	-1.4212	0.2556	0.3177
			0.3								-1.1614	-1.3709	0.2664	0.3349
			0.4								-1.1854	-1.3989	0.2689	0.3385
				0.1							-1.4270	-1.6540	0.2513	0.3137
				0.2							-1.2474	-1.4614	0.2569	0.3214
					$\pi/6$						-1.0973	-1.2918	0.2625	0.3300
					$\pi/4$						-1.0901	-1.2812	0.2635	0.3318
						0.2					-1.1382	-1.3519	0.2569	0.3200
						0.3					-1.1638	-1.3893	0.2534	0.3136
							0.1				-1.1112	-1.3124	0.2760	0.3500
							0.3				-1.1112	-1.3124	0.2452	0.3032
								0.1			-1.1112	-1.3124	0.2268	0.2835
								0.5			-1.1112	-1.3124	0.2925	0.3674
									0.1		-1.1112	-1.3124	0.1397	0.1760
									0.3		-1.1112	-1.3124	0.3664	0.4569
										0.2	-1.1112	-1.3124	0.2522	0.3138
										0.3	-1.1112	-1.3124	0.2358	0.2894

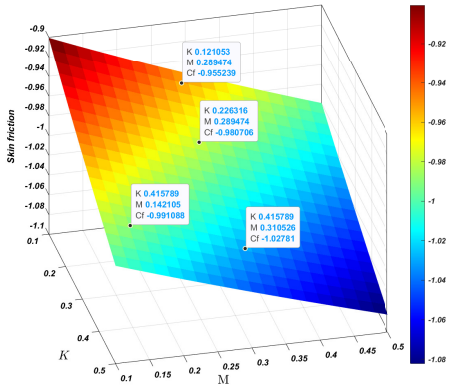

FIGURE 4. Skin friction against K and M

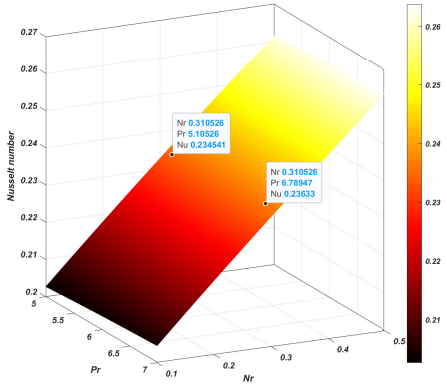

FIGURE 5. Nusselt number against Nr and Pr

Figure 7 demonstrates the response of the velocity field to variations in the magnetic parameter M. An increase in M corresponds to a stronger externally applied magnetic field, which induces a Lorentz force that opposes fluid motion. This electromagnetic damping effect leads to a decline in velocity for both fluid types. From a physical perspective, the interaction between the induced electric current and the applied magnetic field generates resistive forces that convert a portion of kinetic energy into thermal energy, thereby retarding fluid motion. However, the hybrid nanofluid exhibits greater resistance to this suppression, maintaining a higher velocity profile than the Cu-SA nanofluid. This is because the graphene oxide nanoparticles enhance electrical and thermal conductivity, facilitating improved energy transport and enabling the fluid to withstand magnetic drag more effectively. Such

TABLE 5. Computational outcomes of Sherwood number $Sh_x Re_x^{1/2}$ with respect to several important parameters.

λ	S	K	A	Λ	Υ	M	Sc	K_1	$Sh_x Re_x^{\frac{1}{2}}$ Cu-SA	$Sh_x Re_x^{\frac{1}{2}}$ GO-Cu/SA
0.1	0.1	0.1	0.1	0.3	$\pi/2$	0.1	0.3	0.2	0.4031	0.4492
0.2									0.3863	0.4482
0.3									0.3854	0.4472
	0.2								0.4060	0.4749
	0.3								0.4257	0.5018
		0.3							0.3818	0.4413
		0.4							0.3795	0.4379
			0.3						0.3519	0.4063
			0.4						0.3344	0.3849
				0.1					0.4006	0.4669
				0.2					0.3931	0.4572
					$\pi/6$				0.3893	0.4526
					$\pi/4$				0.3886	0.4514
						0.2			0.3843	0.4449
						0.3			0.3817	0.4411
							0.5		0.5151	0.6074
							0.7		0.6314	0.7483
								0.1	0.3317	0.3859
								0.3	0.4362	0.5048

behavior is important in magnetohydrodynamic (MHD) applications, including cooling of electronic devices and plasma flow control, where stability under strong magnetic fields is desirable.

Figure 8 highlights the effect of the suction parameter S on the velocity distribution within the boundary layer. As the value of S increases, a noticeable reduction in the velocity profile is observed for both the nanofluid and the hybrid nanofluid. This reduction occurs because stronger suction at the surface tends to withdraw fluid particles toward the wall, which compresses the boundary layer and suppresses fluid motion. Physically, suction reduces the thickness of the velocity boundary layer, enhancing momentum transfer to the wall but at the expense of bulk flow velocity. This mechanism is often exploited in boundary-layer control techniques to delay flow separation over aerodynamic surfaces. Despite this suppression, the hybrid nanofluid `GO-Cu/SA` consistently retains a higher velocity compared to the monofluid `Cu/SA`, indicating that the hybrid composition supports better momentum transport even under adverse suction conditions.

Figure 9 illustrates the impact of the velocity slip parameter Λ on the fluid flow. An increase in Λ reduces the no-slip condition at the wall, allowing the fluid to slip past the surface, which weakens the shear interaction between the fluid and the boundary. As a result, a decrease in velocity is noted throughout the flow domain. In practical terms, velocity slip is highly relevant in micro- and nano-scale fluid systems where rarefaction effects or hydrophobic coatings weaken the fluid–surface interaction. The reduction is more pronounced for the monofluid, whereas the hybrid nanofluid continues to maintain a relatively thicker momentum boundary layer. This behavior reflects the superior transport characteristics and structural stability of the hybrid nanofluid, making it more suitable for microfluidic applications where slip effects are unavoidable.

From a practical viewpoint, such behavior is crucial in solar-powered aircraft applications, where effective control of boundary layer characteristics can enhance aerodynamic performance and thermal management. The hybrid nanofluid's ability to sustain higher velocity and thicker boundary layers even under adverse slip or suction conditions underscores its suitability for high-performance aerospace thermal systems.

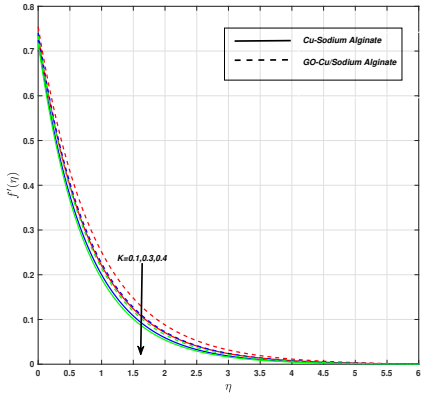

FIGURE 6. Velocity field against K

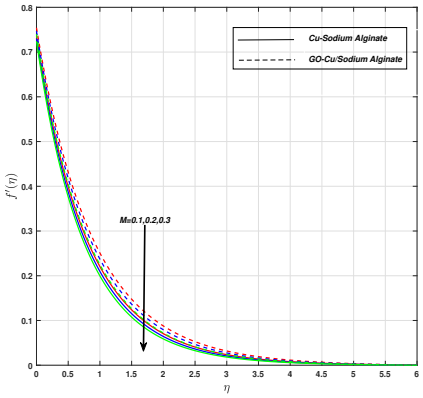

FIGURE 7. Velocity field against M

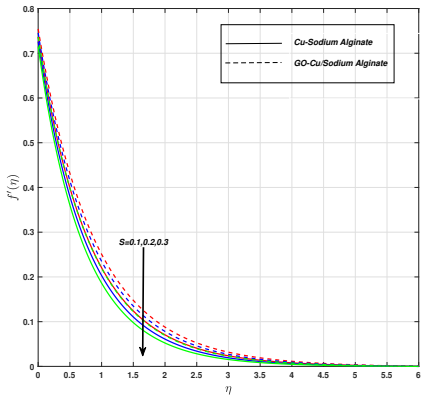

FIGURE 8. Velocity field against S

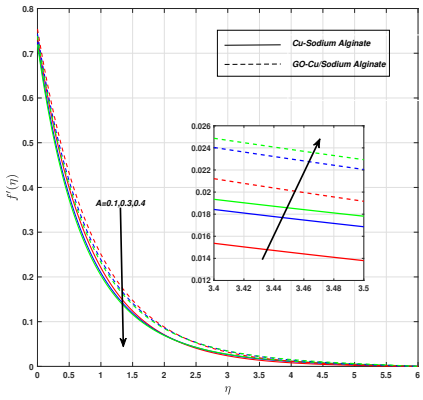

FIGURE 9. Velocity field against A

5.3. **Thermal field.** Figure 10 highlights the effect of the heat generation parameter Q on the thermal behavior of both the nanofluid (`Cu/SA`) and hybrid nanofluid (`GO-Cu/SA`) models. An increase in Q causes a substantial rise in the temperature profile due to internal heat sources that inject additional thermal energy into the system. Physically, this represents situations where exothermic chemical reactions or volumetric heat generation occur, supplying heat directly into the flow. Notably, the hybrid nanofluid exhibits a more pronounced thermal response, reflecting its superior ability to absorb and retain heat. This is evident from the broader thermal boundary layer of the `GO-Cu/SA`-based Williamson fluid, which surpasses that of the `Cu/SA` fluid. The enhanced thermal behavior arises from the synergistic effect of graphene oxide and copper nanoparticles, which improve lattice vibrations and electron

transport, thereby intensifying conduction mechanisms within the fluid. This makes hybrid nanofluids more suitable for energy-intensive applications such as nuclear cooling or high-performance heat exchangers where internal heating is dominant.

Figure 11 demonstrates the influence of the Biot number Bi on the temperature distribution within the boundary layer. An increasing Biot number corresponds to stronger convective heating at the surface, resulting in elevated temperatures throughout the fluid. For smaller values of Bi, the heat exchange at the surface is minimal, producing a nearly uniform temperature field. In contrast, a higher Biot number signifies a thermally thick regime, where substantial temperature gradients develop near the surface, enhancing the thermal boundary layer. From a physical viewpoint, the Biot number characterizes the relative importance of surface convection to internal conduction. When Bi is large, heat penetrates deeply into the fluid, creating steep gradients that intensify entropy generation. This parameter is particularly important in applications like solar aircraft skin surfaces, thermal coatings, or solar collectors, where efficient heat absorption at the surface must be balanced with minimizing internal thermal stresses.

In Figure 12, the effect of the Eckert number Ec on the temperature profile is displayed. An increase in Ec implies stronger viscous dissipation effects, wherein mechanical energy is irreversibly transformed into thermal energy. This mechanism is especially relevant at high velocities or in flows with strong shear, where fluid friction contributes a measurable heating effect. This phenomenon contributes additional heat to the fluid system, thereby elevating its temperature. The hybrid nanofluid again demonstrates higher thermal energy retention compared to its monofluid counterpart, highlighting its capacity to tolerate and redistribute thermal loads under conditions of intense mechanical work. Such characteristics are advantageous in aerospace boundary layers, high-speed lubrication films, and turbomachinery cooling.

Figure 13 captures the influence of the thermal radiation parameter R on the temperature field. A higher value of R enhances radiative heat transfer within the fluid, leading to an overall temperature rise. This behavior is governed by three primary mechanisms: (i) facilitation of heat transmission through the boundary layer via radiation, (ii) increased absorption and redistribution of thermal energy by highly conductive nanoparticles, and (iii) the reinforcement of internal energy transport through both conduction and radiation modes. In practical terms, higher R simulates high-temperature environments such as combustion chambers, re-entry vehicles, or solar thermal systems, where radiation becomes a dominant mode of energy transfer. Between the two fluids, the hybrid nanofluid sustains a comparatively elevated temperature profile due to its greater radiative and conductive heat transfer capabilities, demonstrating its suitability for extreme thermal environments where both conduction and radiation strongly interact.

5.4. **Concentration field.** Figure 14 illustrates the influence of the chemical reaction parameter K_1 on the concentration distribution within the boundary layer. As K_1 increases, a notable reduction in the concentration profile is observed for both nanofluid and hybrid nanofluid models. This behavior is attributed to the enhanced rate of reactive consumption of solute species when K_1 rises, resulting in a diminished solute presence within the flow domain. Physically, a stronger chemical reaction accelerates the depletion of solute molecules through reaction kinetics, which not only reduces their diffusion into the bulk fluid but also weakens species transport away from the wall. Consequently, the concentration boundary layer becomes thinner, indicating stronger irreversibility in mass transport. The impact of the Schmidt number (Sc) on solute concentration is presented in Figure 15. It is evident that increasing Sc leads to a suppression of the concentration profile. Since Sc represents the ratio of momentum diffusivity to mass diffusivity, a higher Sc implies reduced mass diffusivity. This reduction limits the

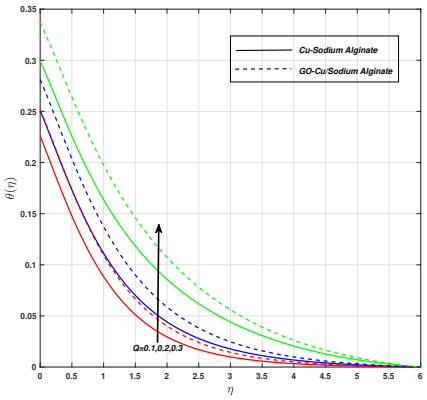

FIGURE 10. Thermal field against Q

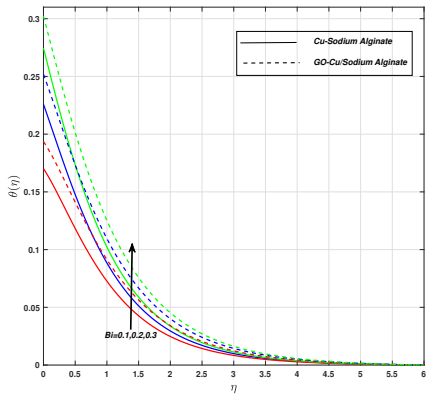

FIGURE 11. Thermal field against Bi

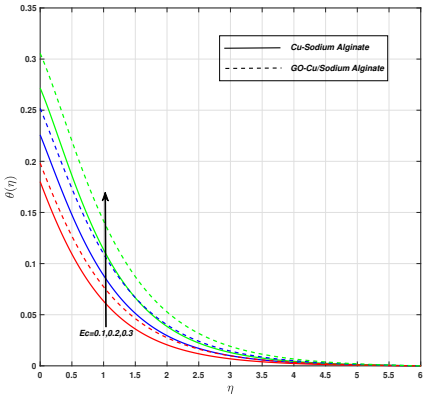

FIGURE 12. Thermal field against Ec

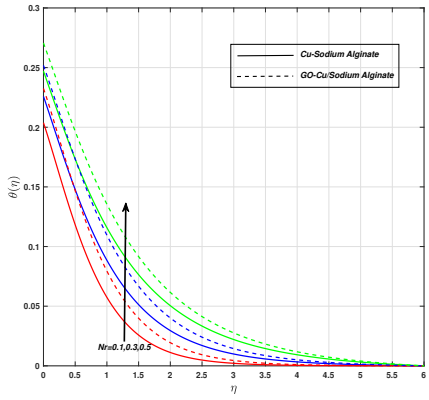

FIGURE 13. Thermal field against Nr

capacity of the solute to spread across the boundary layer, confining its distribution closer to the surface and hence lowering the overall concentration profile.

In the context of solar aircraft systems, where precise control over reactive mass transport is crucial for material efficiency and system performance, understanding these parametric influences helps optimize thermal and mass transport processes, especially in high-altitude operational environments.

5.5. **Motile microorganisms.** Figure 16 presents the variation in motile microorganism distribution $\chi(\eta)$ under the influence of the Peclet number (Pe). A consistent rise in the motile microorganism profile is observed with increasing Pe for both the `Cu/SA` nanofluid and the `GO-Cu/SA` hybrid nanofluid. Physically, a higher Peclet number signifies that the convective transport of microorganisms dominates over diffusive effects, allowing microorganisms to be advected more efficiently toward the flow direction. This leads to an accumulation of microorganisms in the flow region, enhancing the density profile across the boundary layer.

On the other hand, Figure 17 illustrated that the impact of the bioconvection Lewis number (Lb) shows a contrary effect. With the increase in Lb, a decline in the microorganism profile is noted. This

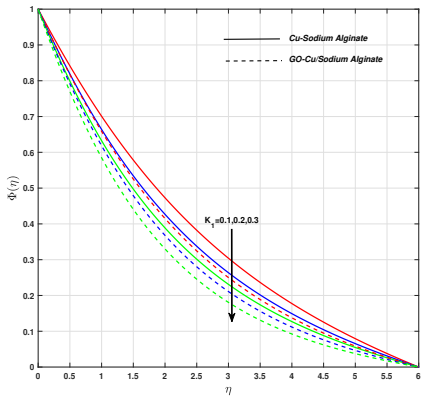

FIGURE 14. Concentration field against K_1

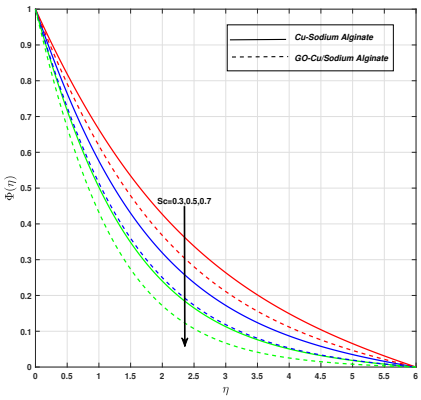

FIGURE 15. Concentration field against Sc

parameter characterizes the relative diffusivity of the motile microorganisms compared to nanoparticles. An elevated Lb indicates that microorganisms disperse more rapidly, resulting in a less concentrated distribution. This dispersion weakens the localized density of motile organisms and ultimately reduces the strength of bioconvective currents.

In comparing the two working fluids, the `Cu/SA` nanofluid consistently exhibits a higher microorganism density profile than the `GO-Cu/SA` hybrid nanofluid. This distinction due to the additional interactions in the hybrid nanofluid that tend to resist microorganism accumulation due to altered flow characteristics and enhanced thermal conductivity. The presence of graphene oxide and copper particles modifies the microenvironment, thereby slightly suppressing the bio-convective activity.

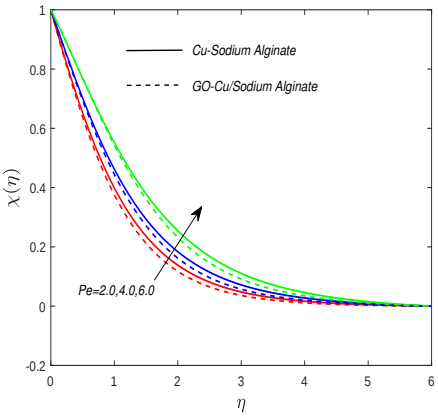

FIGURE 16. Density impact against Pe

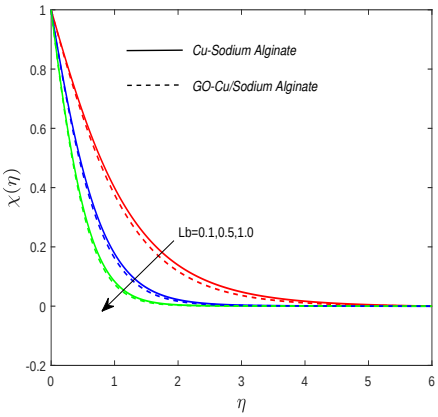

FIGURE 17. Density impact against Lb

5.6. **Entropy analysis.** Figure 18 demonstrates that entropy generation increases with the Reynolds number (Re). Physically, a higher Reynolds number signifies enhanced inertial forces within the flow, which intensify velocity gradients and hence viscous dissipation. This results in greater irreversible losses due to frictional heating, contributing to higher entropy production. In practical terms, larger

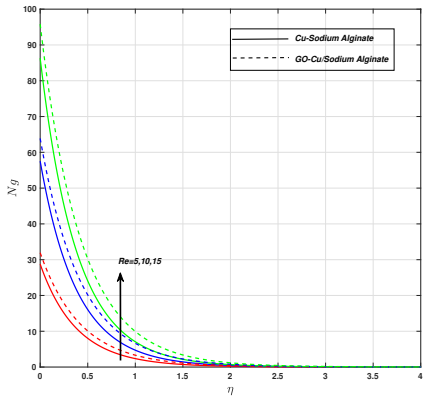

FIGURE 18. Entropy against Re

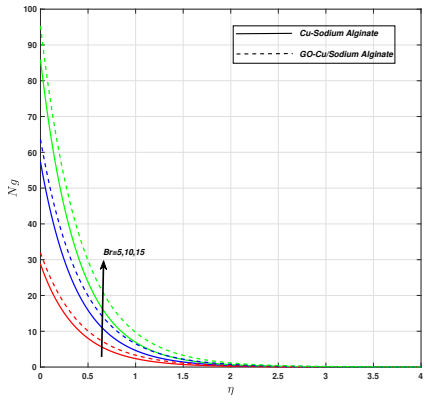

FIGURE 19. Entropy against Br

Re corresponds to higher flow rates, which not only increase turbulence intensity and mixing but also amplify frictional resistance within the boundary layer. This coupling of inertial and dissipative mechanisms explains why entropy rises more rapidly in hybrid nanofluids, whose suspended particles introduce additional micro-level momentum exchange and inter-particle collisions.

In Figure 19, the impact of the Brinkman number (Br) on entropy generation is displayed. A noticeable rise in entropy is observed with increasing Br, which is expected since this parameter characterizes the ratio of viscous dissipation to conductive heat transfer. As viscous heating intensifies, the system deviates further from thermodynamic equilibrium, resulting in amplified entropy production. This is particularly significant in high-speed and high-temperature aerospace systems, where such dissipative effects are pronounced. Conversely, the effect of the velocity slip parameter (Λ) reveals a mitigating influence on entropy generation, as depicted in Figure 20. As Λ increases, the no-slip boundary condition weakens, leading to a reduction in shear stress at the fluid-surface interface. This, in turn, lowers the viscous dissipation rate, thus reducing entropy generation. From a physical perspective, introducing slip effectively relaxes momentum transfer between the fluid and the solid boundary, leading to smoother flow near the wall and reduced frictional heating. Interestingly, the decline is more substantial in the case of the `Cu/SA` nanofluid, suggesting that hybrid nanofluids sustain higher resistance to entropy reduction because the embedded `GO-Cu` particles reinforce interfacial interactions, even under slip conditions.

Overall, the `GO-Cu/SA` hybrid nanofluid consistently shows a higher entropy generation profile than `Cu/SA` across all parameter variations. This trend underscores the dual nature of hybrid nanofluid, while they enhance thermal transport, they also introduce additional irreversibility due to intensified micro-level interactions. From a design perspective, this trade-off must be carefully managed when utilizing such fluids in solar-powered aircraft systems to ensure optimal thermal efficiency and energy conservation.

6. Conclusion

This study presents a comparative analysis of `Cu/SA` nanofluid and `GO-Cu/SA` hybrid nanofluid within a bio-convective Williamson model, including effects of inclined magnetic fields, radiation, velocity slip, and chemical reactions. The outcomes are highly relevant for optimizing thermal systems in solar-powered aircraft. Key findings are as follows:

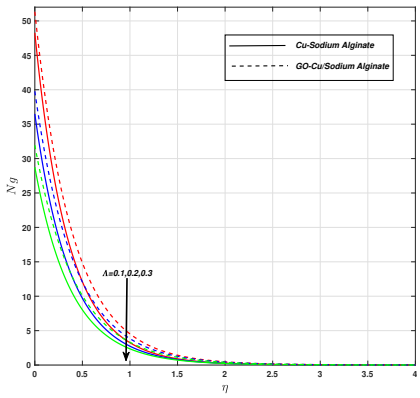

FIGURE 20. Entropy against Λ

- Skin friction increases with suction and magnetic field effects, improving boundary layer stability and surface control in high-speed aerial flows.
- Under varying Biot numbers, heat transfer rose dramatically by 40.60-86.54% in nanofluid and 39.90-85.67% in hybrid nanofluid, highlighting the role of convective heating in wing-mounted solar collectors.
- Hybrid nanofluid exhibits superior thermal performance compared to nanofluid, due to enhanced conductivity from combined `Cu` and `GO` nanoparticles, crucial for managing solar heat loads in wing-integrated collectors.
- Heat transfer rate increased by 14.90% in nanofluid and 15.20% in hybrid nanofluid due to thermal conductivity improvements, vital for managing concentrated solar loads on wing surfaces.
- Chemical reactions boost mass transfer, which is beneficial in applications involving airborne chemical sensors or catalytic fuel systems.
- Entropy generation decreases with velocity slip, suggesting improved energy efficiency and reduced thermal losses in advanced aerospace heat exchangers.

7. Practical Implications

The present study on sodium alginate `(SA)`-based mono-nanofluid and hybrid nanofluid highlights their significant practical applications in advanced thermal management systems. The enhanced heat transfer characteristics of these fluids make them promising candidates for use in solar-powered aircraft, solar energy harvesting, and solar-electric hybrid propulsion modules. Furthermore, their effectiveness in high-performance thermal systems is crucial for maintaining precise temperature control in solar aircraft operating under intense solar radiation.

8. Future Interest

The findings of the current study can serve as a foundation for future advancements by incorporating more generalized transport models. In particular, the inclusion of non-Fourier and non-Fick's laws would allow the consideration of time delays in heat and mass transfer processes, providing a more realistic depiction of thermal and solutal behavior in advanced aerospace systems. Additionally, the implementation of a thermal slip condition could further enhance the understanding of boundary heat

transfer mechanisms and improve the predictive accuracy for the efficiency and performance of solar-powered heating systems.

Data Availability Statement. No Data associated in the manuscript.

References

[1] F. Abbas, H. M. Ali, M. Shaban, M. M. Janjua, T. R. Shah, M. H. Doranehgard, M. Ahmadlouydarab and F. Farukh, *Towards convective heat transfer optimization in aluminum tube automotive radiators: Potential assessment of novel Fe_2O_3–TiO_2/water hybrid nanofluid*, J. Taiwan Inst. Chem. Eng., **124**(2021), 424–436.

[2] A. S. Abdelrazik, R. Saidur and F. A. Al-Sulaiman, *Investigation of the performance of a hybrid PV/thermal system using water/silver nanofluid-based optical filter*, Energy, **215**(2021): 119172.

[3] M. AbuGhanem, P. B. Raafat, F. N. Ibrahim, M. A. Zaky and A. S. Hendy, *Comparative characterization of entropy and heat transfer in carbon-based magnetohydrodynamic Cross nanofluids flowing through PTSCs: advancing thermal applications for solar-powered aircraft*, Int. J. Model. Simul., **2024**(2024), 1–26.

[4] B. Ali, Y. Nie, S. A. Khan, M. T. Sadiq and M. Tariq, *Finite element simulation of multiple slip effects on MHD unsteady Maxwell nanofluid flow over a permeable stretching sheet with radiation and thermo-diffusion in the presence of chemical reaction*, Processes, **7**(2019): 628.

[5] T. Armaghani, M. S. Sadeghi, A. M. Rashad, M. A. Mansour, A. J. Chamkha, A. S. Dogonchi and H. A. Nabwey, *MHD mixed convection of localized heat source/sink in an Al_2O_3–Cu/water hybrid nanofluid in L-shaped cavity*, Alex. Eng. J., **60**(2021), 2947–2962.

[6] A. Bejan, *Entropy generation minimization: The method and its applications*, Thermal Sciences 2000: Proc. Int. Thermal Sci. Seminar, Vol. 1, Begel House Inc., 2000.

[7] K. Bashirnezhad, M. Kargaran, S. Z. Heris, Y. Mohammadfam, *Improvement of thermal, energy and exergy performance of flat panel solar collector by insertion of perforated strips and hybrid CuO-MWCNTs nanofluid*, Results Eng., **27** (2025): 106120.

[8] A. Boroomandpour, D. Toghraie and M. Hashemian, *A comprehensive experimental investigation of thermal conductivity of a ternary hybrid nanofluid containing MWCNTs–titania–zinc oxide/water–ethylene glycol (80:20) as well as binary and mono nanofluids*, Synth. Met., **268**(2020): 116501.

[9] R. L. Burden and J. D. Faires, *Numerical Analysis*, Brooks/Cole, Cengage Learning, Boston, 2011.

[10] P. Campbell, Y. Zhang, F. Yan, Z. Lu and D. Streets, *Impacts of transportation sector emissions on future US air quality in a changing climate. Part I: Projected emissions, simulation design, and model evaluation*, Environ. Pollut., **238**(2018): 903–917.

[11] S. U. S. Choi and J. A. Eastman, *Enhancing thermal conductivity of fluids with nanoparticles*, Argonne National Laboratory Report, Argonne, IL, 1995.

[12] X.-Z. Gao, Z.-X. Hou, Z. Guo, J.-X. Liu and X.-Q. Chen, *Energy management strategy for solar-powered high-altitude long-endurance aircraft*, Energy Convers. Manage., **70**(2013), 20–30.

[13] X.-Z. Gao, Z.-X. Hou, Z. Guo and X.-Q. Chen, *Reviews of methods to extract and store energy for solar-powered aircraft*, Renew. Sustain. Energy Rev., **44**(2015), 96–108.

[14] J.-H. He, G. M. Moatimid, M. A. A. Mohamed and K. Elagamy, *A stretching cylindrical Carreau nanofluid border layer movement with motile microorganisms and variable thermal characteristics*, Int. J. Mod. Phys. B, **38** (2024): 2450223.

[15] G. Huminic and A. Huminic, *The heat transfer performances and entropy generation analysis of hybrid nanofluids in a flattened tube*, Int. J. Heat Mass Transf., **119**(2018), 813–827.

[16] M. Jalil, S. Asghar and S. Yasmeen, *An exact solution of MHD boundary layer flow of dusty fluid over a stretching surface*, Math. Probl. Eng., **2017**(2017), 2307469.

[17] H. Jin, C. Wang and C. Fan, *Simulation study on hydrogen-heating-power poly-generation system based on solar driven supercritical water biomass gasification with compressed gas products as an energy storage system*, J. Therm. Sci., **29**(2020), 365–377.

[18] D. Kashyap and A. K. Dass, *Effect of boundary conditions on heat transfer and entropy generation during two-phase mixed convection hybrid Al_2O_3–Cu/water nanofluid flow in a cavity*, Int. J. Mech. Sci., **157**(2019), 45–59.

[19] R. Khosravi, S. Rabiei, M. Bahiraei and A. R. Teymourtash, *Predicting entropy generation of a hybrid nanofluid containing graphene–platinum nanoparticles through a microchannel liquid block using neural networks*, Int. Commun. Heat Mass Transf., **109**(2019): 104351.

[20] A. V. Kuznetsov and A. A. Avramenko, *Effect of small particles on the stability of bioconvection in a suspension of gyrotactic microorganisms in a layer of finite depth*, Int. Commun. Heat Mass Transf., **31**(2004), 1–10.

[21] A. Khan, Hashim, M. Farooq, M. A. Qureshi, M. Prakash, K. Guedri, B. M. Fadhl, A. H. Almaliki, M. Bayram, *Quadratic mixed convection of Maxwell–Buongiorno nanofluid over cubic stratified surface incorporating cross diffusion effects and solar radiation*, Sci. Rep., **15** (2025): 20092.

[22] H. Maleki, M. R. Safaei, H. Togun and M. Dahari, *Heat transfer and fluid flow of pseudo-plastic nanofluid over a moving permeable plate with viscous dissipation and heat absorption/generation*, J. Therm. Anal. Calorim., **135**(2019), 1643–1654.

[23] S. Majumder, T. Chakraborty and P. K. Kundu, *Framing the influence of solar radiation over entropy generation in unsteady magnetized CNT nanofluid flow possessing variable thermal conductivity over a rotating sphere*, Numer. Heat Transf., Part A: Appl., **2025**(2025), 1–33.

[24] G. O. Ogunsanwo, O. B. Alaba, A. M. Obalalu, A. F. Isarinade, U. Khan, R. Ghodhbani, A. A. Owoade and G. T. Solola, *Dynamics of second-law analysis and thermal performance in solar-powered tractors using a parabolic trough solar collector filled with tri-hybrid nanofluid*, J. Therm. Anal. Calorim., **2025**(2025), 1–16.

[25] P. K. Pattnaik, S. R. Mishra, M. D. Shamshuddin, S. Panda and R. Baithalu, *Significant statistical model of heat transfer rate in radiative Carreau tri-hybrid nanofluid with entropy analysis using response surface methodology used in solar aircraft*, Renew. Energy, **237**(2024): 121521.

[26] F. Rubbi, K. Habib, R. Saidur, N. Aslfattahi, S. M. Yahya and L. Das, *Performance optimization of a hybrid PV/T solar system using Soybean oil/MXene nanofluids as a new class of heat transfer fluids*, Sol. Energy, **208**(2020), 124–138.

[27] S. Rana, R. Mehmood, M. M. Bhatti and M. Hassan, *Swimming of motile gyrotactic microorganisms and suspension of nanoparticles in a rheological Jeffery fluid with Newtonian heating along elastic surface*, J. Cent. South Univ., **28**(2021), 3279–3296.

[28] B. M. Rao, P. Durgaprasad, G. Dharmaiah, S. Dinarvand, S. Gupta, *A multiple applications study of motile microorganisms past a vertical surface with double-diffusive binary base fluid*, Heat Transf., **53** (2024), 4468–4487.

[29] M. Shamshuddin and M. R. Eid, *n-th order reactive nanoliquid through convective elongated sheet under mixed convection flow with joule heating effects*, J. Therm. Anal. Calorim., **147**(2022), 3853–3867.

[30] F. Shahzad, J. Bouslimi, S. Gouadria, W. Jamshed, M. R. Eid, R. Safdar, M. Shamshuddin, and K. S. Nisar, *Hydrogen energy storage optimization in solar-HVAC using Sutterby nanofluid via Koo-Kleinstreuer and Li (KKL) correlations model: A solar thermal application*, Int. J. Hydrogen Energy, **47** (2022), 18877–18891.

[31] F. Shahzad, W. Jamshed, M. R. Eid, R. W. Ibrahim, R. Safdar, K. S. Nisar and M. D. Shamshuddin, *Thermal amelioration in heat transfer rate using Oldroyd-B model hybrid nanofluid by CNTs-based kerosene oil flow in solar collectors applications*, Waves Random Complex Media, **2022**(2022), 1–31.

[32] H. Shahzad and M. Sagheer, *Entropy generation and mass transfer analysis during a radiative magnetized hybrid ferro-nanofluid flow along with higher order chemical reaction*, J. Nanofluids, **13**(2024), 1336–1349.

[33] H. Shahzad and M. Sagheer, *Forchheimer model and generalized Fourier and Fick heat flux in water based Williamson hybrid nanofluid flow over stretched surface under Lorentz force*, Phys. Scr., **100**(2025): 105223.

[34] J. Subramani, P. Sevvel, S. A. Srinivasan *et al.*, *Influence of CNT coating on the efficiency of solar parabolic trough collector using Al_2O_3 nanofluids—a multiple regression approach*, Mater. Today: Proc., **45**(2021), 1857–1861.

[35] M. Shoaib, M. A. Z. Raja, M. T. Sabir, M. Awais, S. Islam, Z. Shah and P. Kumam, *Numerical analysis of 3-D MHD hybrid nanofluid over a rotational disk in presence of thermal radiation with Joule heating and viscous dissipation effects using Lobatto IIIA technique*, Alex. Eng. J., **60**(2021), 3605–3619.

[36] Y. Tong, T. Boldoo, J. H. Mr and H. Cho, *Improvement of photo-thermal energy conversion performance of $MWCNT/Fe_3O_4$ hybrid nanofluid compared to Fe_3O_4 nanofluid*, Energy, **196**(2020): 117086.

[37] D. Thenmozhi, M. E. Rao, B. N. Reddy, J. Arthy, M. Jawad, G. Bognár, W. Abdelfattah, *Influence of Stefan blowing on the flow and heat transfer of non-Newtonian Jeffrey nanofluid over an unsteady stretching sheet*, Results Eng., **26** (2025): 105375.

[38] M. Wu, Z. Shi, T. Xiao, Z. Chen and H. Ang, *Effect of solar cell efficiency and flight condition on optimal flight control and energy performance for Z-shaped wing stratospheric solar aircraft*, Acta Astronaut., **164**(2019), 366–375.

[39] M. Wu, Z. Shi, T. Xiao and H. Ang, *Effect of wingtip connection on the energy and flight endurance performance of solar aircraft*, Aerosp. Sci. Technol., **108**(2021): 106404.

[40] M. Wu, Z. Shi, H. Ang and T. Xiao, *Theoretical study on energy performance of a stratospheric solar aircraft with optimum Λ-shaped rotatable wing*, Aerosp. Sci. Technol., **98**(2020): 105670.

[41] A. Yousaf, M. Imran, S. Yasmin and M. R. Ali, *Numerical assessment of bioconvection in MHD Prandtl nanofluid with gyrotactic motile microorganisms with bio-fuel applications*, Case Stud. Therm. Eng., **52**(2023): 103639.

[42] J. Zada, A. Khan, M. Farooq, A. S. Alsubaie, S. Rezapour, M. Inc, *Computation of stretching disks fluid flow of hybrid nanofluid under the effect of variable magnetic field*, ZAMM–J. Appl. Math. Mech., **105** (2025): e202400114.

M. N. Sani, Department of Mathematics, Capital University of Science and Technology, Islamabad, 44000, Pakistan

Email address: muhammadnaveedsani@gmail.com

M. Sagheer, Department of Mathematics, Capital University of Science and Technology, Islamabad, 44000, Pakistan

Email address: sagheer@cust.edu.pk

H. Shahzad, corresponding author, Department of Mathematics, Capital University of Science and Technology, Islamabad, 44000, Pakistan

Email address: hassan.shahzad@cust.edu.pk, h.shahzad1996@gmail.com

M. Samiullah, corresponding author, Department of Mathematics, Capital University of Science and Technology, Islamabad, 44000, Pakistan

Email address: samisatti148@gmail.com